**Fig. 3.** Approximate timing and location of gas giant formation in a protoplanetary disk. (**Bottom**) The final or "isolation" mass of solid cores (black dots), with spacing between successive cores taken from planet formation simulations (38). (**Top**) The time (thick solid curve) for a core (black dots; vertical dotted lines connect to corresponding core in bottom panel) to become a gas giant (horizontal dotted lines show times for individual protoplanets). We approximate this as the sum of the time for the core to reach its final mass, τ_{core} (thin solid curve), and the time for the core to undergo runaway gas accretion, taken

to be its Kelvin-Helmholtz time (39), τ_{KH} (dashed curve). As in more detailed calculations (40), we find that gas giant formation commences at one particular radius, which for typical parameters lies in or near the Jupiter-Saturn region (in this case at 7 AU and at time τ_{giant} just under 2 My). Giant formation begins in a burst, with several planets growing in rapid succession, then slows down as it spreads to larger and smaller radii. In practice, once an inner hole forms in the gas disk, formation is constrained to progress only outwards.
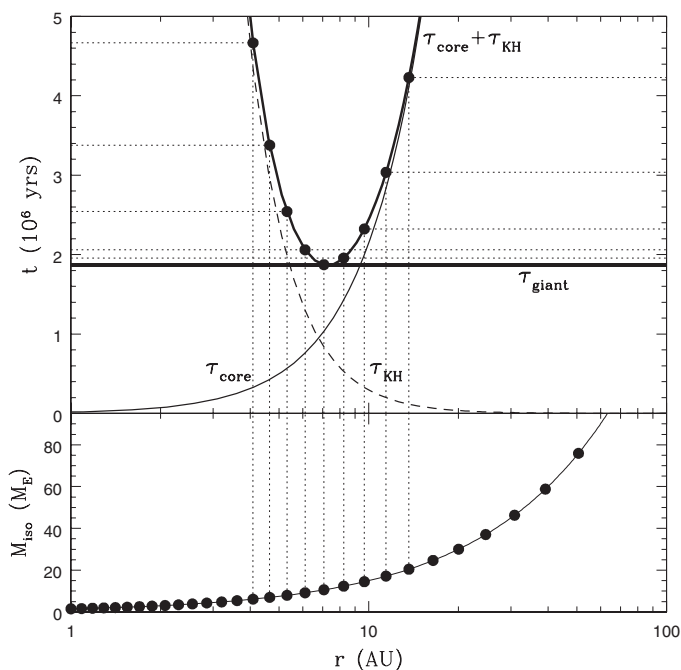
candidates for this scenario). All of this leads us to predict that within the diverse ensemble of planetary systems, ones resembling our own are the exception rather than the rule. Observations may be hinting at this already (30), although the true planet distribution remains largely obscured by selection effects (25). On the other hand, scaled-down versions of the solar system, in which a moderate amount of migration took place, are likely to be more common; indeed, such a system has recently been discovered through microlensing (31). Finally, scenarios in which type II migration is reduced (32, 33) would modify our prediction, permitting a more common occurrence of solar system analogs.

In all of our simulations, the formation of a gas giant brings with it violent scattering of neighboring smaller bodies, including other cores about to undergo runaway gas accretion themselves. Such scattering has been proposed as the origin of Uranus and Neptune (34), with dynamical friction from the remnant outer planetesimal disk (not modeled here) serving to prevent their ejection and ultimately recircularize their orbits. Thus, whether or not Jupiter and Saturn analogs are rare, it is likely that Uranus and Neptune analogs are quite common.

References and Notes

1. K. E. Haisch, E. A. Lada, C. J. Lada, *Astrophys. J.* **553**, L153 (2001).
2. M. Juric, S. Tremaine, *ArXiv Astrophys.*, http://arxiv.org/abs/astroph/0703160 (2007).
3. S. Chatterjee, E. B. Ford, S. Matsumura, F. A. Rasio, *ArXiv Astrophys.*, http://arxiv.org/abs/astroph/0703166 (2007).
4. S. Udry, D. Fischer, D. Queloz, *Protostars and Planets V*, B. Reipurth, D. Jewitt, K. Keil, eds. (2007), pp. 685–699.
5. M. H. Lee, S. J. Peale, *Astrophys. J.* **567**, 596 (2002).
6. P. Goldreich, S. Tremaine, *Astrophys. J.* **241**, 425 (1980).
7. D. N. C. Lin, J. Papaloizou, *Astrophys. J.* **309**, 846 (1986).
8. W. R. Ward, *Icarus* **126**, 261 (1997).
9. S. Ida, D. N. C. Lin, *Astrophys. J.* **604**, 388 (2004).
10. Y. Alibert, C. Mordasini, W. Benz, C. Winisdoerffer, *Astron. Astrophys.* **434**, 343 (2005).
11. J. E. Chambers, *Astrophys. J.* **652**, L133 (2006).
12. S. Ida, D. N. C. Lin, *Astrophys. J.* **673**, 487 (2008).
13. F. C. Adams, G. Laughlin, *Icarus* **163**, 290 (2003).
14. A. T. Lee, E. W. Thommes, F. A. Rasio, *ArXiv Astrophys.*, http://arxiv.org/abs/0801.1926v1 (2008).
15. E. W. Thommes, *Astrophys. J.* **626**, 1033 (2005).
16. M. J. Duncan, H. F. Levison, M. H. Lee, *Astron. J.* **116**, 2067 (1998).
17. E. W. Thommes, L. Nilsson, N. Murray, *Astrophys. J.* **656**, L25 (2007).
18. C. D. Murray, S. F. Dermott, *Solar System Dynamics* (Cambridge Univ. Press, Cambridge, 1999).
19. D. J. Hollenbach, H. W. Yorke, D. Johnstone, *Protostars and Planets IV* (Univ. of Arizona Press, Tucson, AZ, 2000).
20. L. Hartmann, N. Calvet, E. Gullbring, P. D'Alessio, *Astrophys. J.* **495**, 385 (1998).
21. N. I. Shakura, R. A. Syunyaev, *Astron. Astrophys.* **24**, 337 (1973).
22. D. N. C. Lin, P. Bodenheimer, D. C. Richardson, *Nature* **380**, 606 (1996).
23. M. J. Kuchner, M. Lecar, *Astrophys. J.* **574**, L87 (2002).
24. C. Terquem, J. C. B. Papaloizou, *Astrophys. J.* **654**, 1110 (2007).
25. G. Marcy et al., *Prog. Theor. Phys.* **158** (suppl.), 24 (2005).
26. D. A. Fischer, J. A. Valenti, *Scientific Frontiers in Research on Extrasolar Planets*, D. Deming, S. Seager, Eds. (2003), vol. 294 of *Astronomical Society of the Pacific Conference Series*, pp. 117–128.
27. N. C. Santos, G. Israelian, M. Mayor, *Astron. Astrophys.* **415**, 1153 (2004).
28. S. Udry, N. C. Santos, *Annu. Rev. Astron. Astrophys.* **45**, 397 (2007).
29. Scenarios have been proposed in which planets themselves are the source of viscosity (35, 36). Although this would cause the two time scales to be correlated, τ_{giant} would systematically be less than τ_{disk}, thus making substantial migration likely in all planetary systems.
30. M. E. Beer, A. R. King, M. Livio, J. E. Pringle, *Mon. Not. R. Astron. Soc.* **354**, 763 (2004).
31. B. S. Gaudi et al., *Science* **319**, 927 (2008).
32. A. Morbidelli, A. Crida, *Icarus* **191**, 158 (2007).
33. S. Ida, D. N. C. Lin, *ArXiv Astrophys.*, http://arxiv.org/abs/0802.1114 (2008).
34. E. W. Thommes, M. J. Duncan, H. F. Levison, *Nature* **402**, 635 (1999).
35. J. Goodman, R. R. Rafikov, *Astrophys. J.* **552**, 793 (2001).
36. R. Sari, P. Goldreich, *Astrophys. J.* **606**, L77 (2004).
37. C. Hayashi, *Prog. Theor. Phys.* **70**, 35 (1981).
38. E. Kokubo, S. Ida, *Icarus* **131**, 171 (1998).
39. G. Bryden, D. N. C. Lin, S. Ida, *Astrophys. J.* **544**, 481 (2000).
40. M. Ikoma, K. Nakazawa, H. Emori, *Astrophys. J.* **537**, 1013 (2000).
41. We thank the Spitzer Space Telescope Cycle-4 Theoretical Research Program, NSF, and the Natural Sciences and Engineering Research Council of Canada for supporting this work, and two anonymous referees for valuable comments.

Suppressing Spin Qubit Dephasing by Nuclear State Preparation

D. J. Reilly,[1] J. M. Taylor,[2] J. R. Petta,[3] C. M. Marcus,[1]* M. P. Hanson,[4] A. C. Gossard[4]

Coherent spin states in semiconductor quantum dots offer promise as electrically controllable quantum bits (qubits) with scalable fabrication. For few-electron quantum dots made from gallium arsenide (GaAs), fluctuating nuclear spins in the host lattice are the dominant source of spin decoherence. We report a method of preparing the nuclear spin environment that suppresses the relevant component of nuclear spin fluctuations below its equilibrium value by a factor of ~70, extending the inhomogeneous dephasing time for the two-electron spin state beyond 1 microsecond. The nuclear state can be readily prepared by electrical gate manipulation and persists for more than 10 seconds.

Quantum information processing requires the realization of interconnected, controllable quantum two-level systems (qubits) that are sufficiently isolated from their environment that quantum coherence can be maintained for much longer than the characteristic operation time. Electron spins in quantum dots are an appealing candidate system for this application, as the spin of the electron is typically only weakly coupled to the environment relative to the

charge degree of freedom (*1*). Logical qubits formed from pairs of spins provide additional immunity from collective dephasing, forming a dynamical decoherence-free subspace (*2*, *3*).

Implementing any spin-qubit architecture requires the manipulation (*4–6*) and detection (*7*, *8*) of few-electron spin states, as yet demonstrated only in III-V semiconductor heterostructure devices such as gallium arsenide (GaAs), which in all cases comprise atoms with nonzero nuclear spin. The nuclear spins of the host lattice couple to electrons via the hyperfine interaction and causes rapid electron spin dephasing. In the GaAs devices presented here, for instance, an ensemble of initialized spin pairs will retain their phase relationship for $T_2^* \sim 15$ ns, consistent with theoretical estimates (*9–11*) and previous measurements (*4*). The time T_2^* represents an inhomogeneous dephasing time and can be extended with the use of spin-echo methods (*4*). Nonetheless, extending T_2^* by nuclear state preparation considerably reduces the burden of using complex pulse sequences or large field gradients to overcome the influence of fluctuating hyperfine fields when controlling spin qubits.

Proposals to reduce dephasing by nuclear state preparation include complete nuclear polarization (*12*), state-narrowing of the nuclear distribution (*12–15*), and schemes for decoupling the bath dynamics from the coherent evolution of the electron spin through the use of control pulses (*16–18*). These approaches remain largely unexplored experimentally, although recent optical experiments (*19*) have demonstrated a suppression of nuclear fluctuations in ensembles of self-assembled quantum dots.

We demonstrate a nuclear state preparation scheme in a double quantum-dot system, using an electron-nuclear flip-flop pumping cycle controlled by voltages applied to electrostatic gates. Cyclic evolution of the two-electron state through the resonance between the singlet (*S*) and $m_s = 1$ triplet (T_+) (*20*), in the presence of a small (few mT) applied magnetic field, leads to a factor of 70 suppression of fluctuations below thermal equilibrium of the hyperfine field gradient between the dots along the total field direction. It is this component of the hyperfine field gradient that is responsible for dephasing of the two-electron spin qubit formed by *S* and $m_s = 0$ triplet (T_0) states (*4*). Consequently, although the flip-flop cycle generates only a modest net nuclear polarization (<1%), the resulting nuclear state extends T_2^* of the S-T_0 qubit from 15 ns to beyond 1 μs. Once prepared, this nonequilibrium nuclear state persists for ~15 s, eventually recovering equilibrium fluctuations on the same time scale as the re-

[1]Department of Physics, Harvard University, Cambridge, MA 02138, USA. [2]Department of Physics, Massachusetts Institute of Technology, Cambridge, MA 02139, USA. [3]Department of Physics, Princeton University, Princeton, NJ 08544, USA. [4]Materials Department, University of California, Santa Barbara, CA 93106, USA.

*To whom correspondence should be addressed. E-mail: marcus@harvard.edu

Fig. 1. (**A**) Schematic of the energy levels of the two-electron system in a magnetic field. Detuning, ε, from the (2,0)-(1,1) charge degeneracy is gate-controlled. (**B**) Gate-pulse sequence used to separately probe the longitudinal ($\Delta B_n^{\parallel}$, green dashed line) and transverse ($\Delta B_n^{\perp}$, red dashed line) components of the Overhauser field difference, depending on the position of the separation point S. (**C** and **D**) Time-averaged charge-sensing signal V_{rf} from the rf-QPC as a function of gate voltages V_L and V_R, showing features corresponding to the singlet mixing with T_0 [bracketed green triangle in (C)] and T_+ [bracketed green line segment in (D)]. (**E**) Schematic view of the S-T_+ anticrossing, illustrating the pumping cycle. With each iteration of this cycle, with period $\tau_C = 250$ ns, a new singlet state is taken adiabatically through the S-T_+ anticrossing in a time $\tau_A = 50$ ns, then returned nonadiabatically to (2,0) in ~1 ns, where the S state is then reloaded.
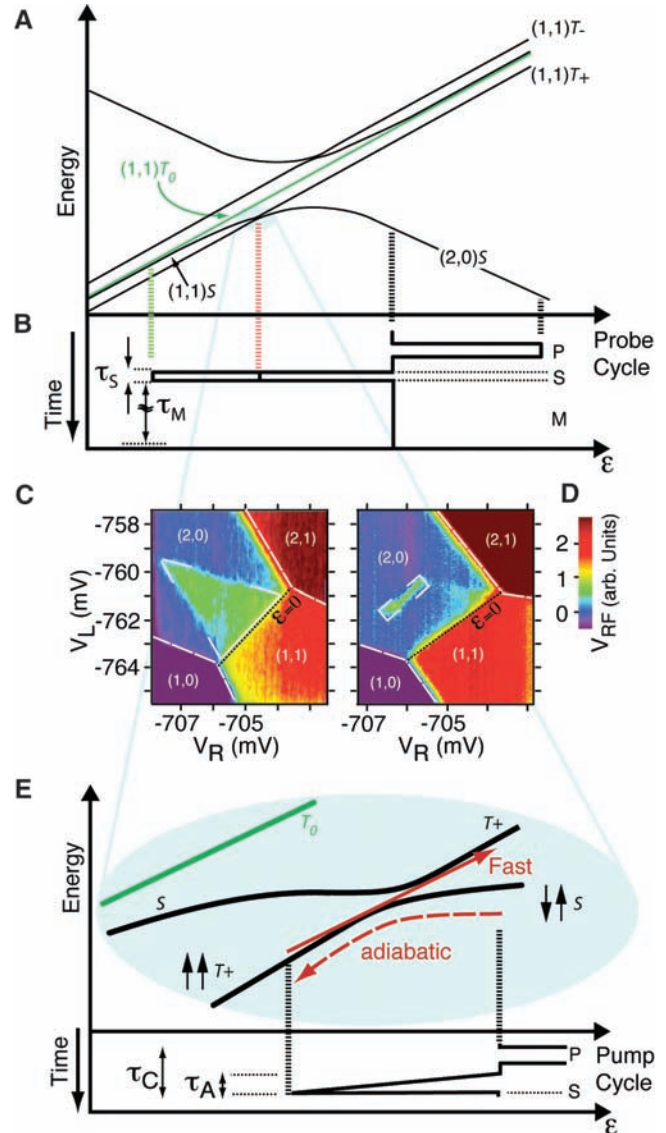
laxation of the small induced nuclear polarization. This recovery time is longer than typical gate operation times by ~9 to 10 orders of magnitude. We propose that occasional nuclear state preparation by these methods may provide a remedy to hyperfine-mediated spin dephasing in networks of interconnected spin qubits.

The double quantum dot is defined in a GaAs-AlGaAs heterostructure with a two-dimensional electron gas (2DEG) 100 nm below the wafer surface (density 2×10^{15} m^{-2}, mobility 20 m^2 V^{-1} s^{-1}). Negative voltages applied to Ti-Au gates create a tunable double-well potential that is tunnel-coupled to adjacent electron reservoirs (fig. S1). A proximal radio-frequency quantum point contact (rf-QPC) senses the charge state of the double dot, measured in terms of the rectified sensor output voltage V_{rf} (*21*). Measurements were made in a dilution refrigerator at a base electron temperature of 120 mK.
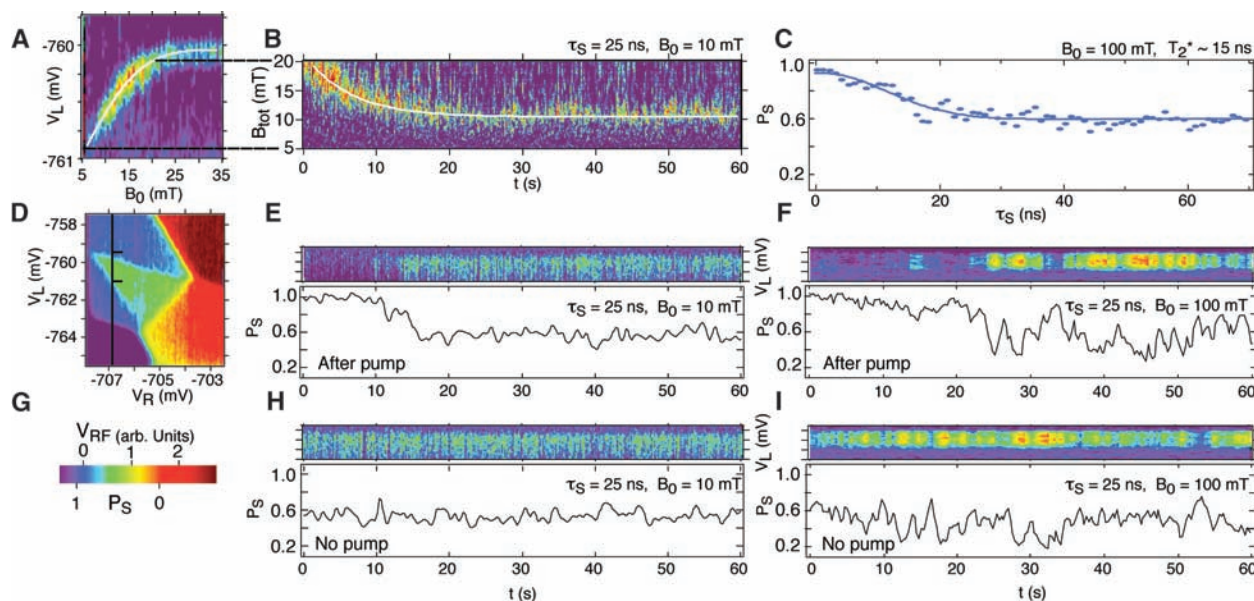
A schematic energy-level diagram (Fig. 1A), with (*n,m*) indicating equilibrium charge occupancies of the left and right dots, shows the three

(1,1) triplet states (T_+, T_0, T_-) split by a magnetic field B_0 applied perpendicular to the 2DEG. The detuning, ε, from the (2,0)-(1,1) degeneracy is controlled by high-bandwidth gate voltage pulses. The ground state of (2,0) is a singlet, with the (2,0) triplet out of the energy range of the experiment.

Each confined electron interacts with $N \sim 10^6$ nuclei via hyperfine coupling, giving rise to a spatially and temporally fluctuating effective magnetic (Overhauser) field (*9–11*, *22*). In the separated (1,1) state, precession rates for the two electron spins depends on their local effective fields, which can be decomposed into an average field and a difference field. It is useful to resolve $\mathbf{B}_n = (\mathbf{B}_n^l + \mathbf{B}_n^r)/2$, the Overhauser part of the total average field, $\mathbf{B}_{tot} = \mathbf{B}_0 + \mathbf{B}_n$, into components along ($B_n^{\parallel}$) and transverse ($B_n^{\perp}$) to $\mathbf{B}_{tot}$. The difference field, due only to Overhauser contributions, is given by $\Delta\mathbf{B}_n = (\mathbf{B}_n^l - \mathbf{B}_n^r)/2$, with components along ($\Delta B_n^{\parallel}$) and transverse ($\Delta B_n^{\perp}$) to $\mathbf{B}_{tot}$. At large negative ε, where the two electrons are well separated and exchange $J(\varepsilon)$ is negligible, $\Delta B_n^{\parallel}$ sets the precession rate between

Fig. 2. (**A**) Position of the S-T_+ resonance in left-dot gate voltage V_L as a function of applied magnetic field amplitude B_0, without prior pump cycle. (**B**) Evolution of the S-T_+ position as a function of time. Vertical scale is converted from gate voltage V_L to B_{tot} via the resonance position in (A). Resonance position in gate voltage V_L and converted to B_{tot} via (A). (**C**) Singlet return probability P_S as a function of τ_S at $B_0 = 100$ mT. Gaussian fit gives an inhomogeneous dephasing time $T_2^* = 15$ ns. (**D**) Sensor output V_{rf}, as in Fig. 1C, showing triangle that yields P_S. Vertical cut (black line) with tick marks shows location of slices in upper panels of (E) to (I). (**E** and **F**) After the pump cycle, repeated slices across this triangle at the position indicated by the black line in (D) allow a calibrated measure of P_S as it evolves in time, at (E) $B_0 = 10$ mT and (F) $B_0 = 100$ mT. (**G**) Calibration between the sensing signal V_{rf} and singlet return probability P_S. (**H** and **I**) Control experiments showing slices across the triangle as in (E) and (F), but without a prior pump cycle.
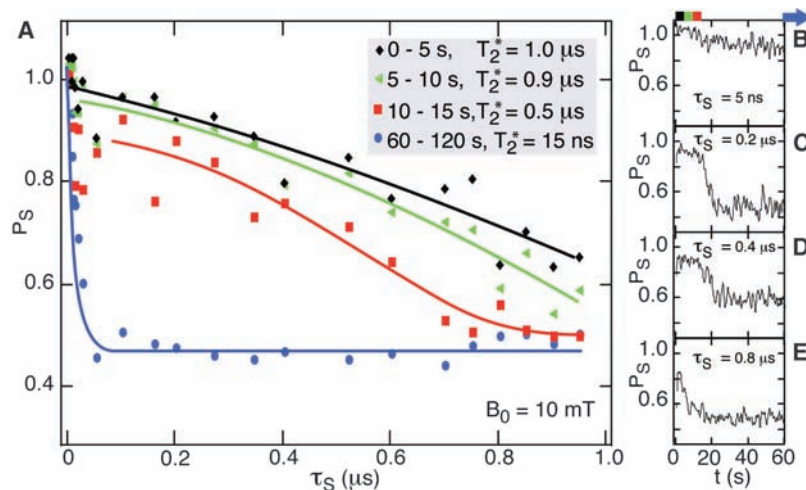
Fig. 3. (**A**) Singlet return probability P_S as a function of separation time τ_S deep in (1,1) (green dashed line in Fig. 1A), where S mixes with T_0. P_S values are shown averaged within the 0- to 5-s interval (black), the 5- to 10-s interval (green), the 10- to 15-s interval (red), and 60 to 120 s after the pump cycle (blue), along with Gaussian fits. (**B** to **E**) P_S as a function of time following the pump cycle ($B_0 = 10$ mT) for fixed $\tau_S = 5$ ns (B), $\tau_S = 0.2$ μs (C), $\tau_S = 0.4$ μs (D), and $\tau_S = 0.8$ μs (E).

S and T_0 states. At the value of detuning where $J(\varepsilon)$ equals the Zeeman energy $E_Z = g\mu_B B_{tot}$ (where g is the electron g factor and μ_B is the Bohr magneton), precession between S and T_+ states occurs at a rate set by $\Delta B_n^\perp$.

For measurement of the precession or dephasing of spin pairs in the two dots, a gate-pulse cycle ("probe cycle") first prepares (P) a singlet state in (2,0), then separates (S) the two electrons into (1,1) for a duration τ_S, then measures (M) the

probability of return to (2,0). States that evolve into triplets during τ_S remain trapped in (1,1) by the Pauli blockade and are detected as such by the rf-QPC charge sensor (4). Figure 1, C and D, shows the time-averaged charge-sensing signal V_{rf} as a function of constant offsets to gate biases V_L and V_R, with this pulse sequence running continuously. Setting the amplitude of the S-pulse to mix S with T_0 at large detuning (green dashed line, Fig. 1B) yields the "readout triangle" indi-

cated in Fig. 1C. Within the triangle, V_{rf} is between (2,0) and (1,1) sensing values, indicating that for some probe cycles the system becomes Pauli-blockaded in (1,1) after evolving to a triplet state. Outside this triangle, alternative spin-independent relaxation pathways circumvent the blockade (23). For a smaller-amplitude S-pulse (red dashed line, Fig. 1B), S mixes with T_+, also leading to partial Pauli blockade and giving the narrow resonance feature seen in Fig. 1D. The dependence of the S-T_+ resonance position on applied field B_0 serves as a calibration, mapping the gate voltage V_L (at fixed V_R) into the total effective field B_{tot}, including possible Overhauser fields (Fig. 2A). The charge-sensing signal V_{rf} is also calibrated using equilibrium (1,1) and (2,0) sensing values to give the probability $1 - P_S$ that an initialized singlet will evolve into a triplet during the separation time τ_S (Fig. 2G). A fit to $P_S(\tau_S)$ (Fig. 2C) yields (11, 22, 24) a dephasing time $T_2^* = (h/2\pi)/g\mu_B\langle\Delta B_n^\parallel\rangle_{rms} \sim 15$ ns, where h is Planck's constant and the subscript rms denotes a root-mean-square time-ensemble average.

We now investigate effects of the electron-nuclear flip-flop cycle ("pump cycle") (Fig. 1E). Each iteration of the pump cycle moves a singlet, prepared in (2,0), adiabatically through the S-T_+ resonance, then returns nonadiabatically to (2,0), where the state is re-initialized to a singlet by exchanging an electron with the adjacent reservoir (20). In principle, with each iteration of this cycle, a change in the angular momentum of the electron state occurs, with a corresponding change to the nuclear system. Iterating the pump cycle at

819

4 MHz creates a modest nuclear polarization on the order of 1%, as seen previously [20]. The pump cycle was always iterated for more than 1 s, and no dependence on pumping time beyond 1 s was observed. What limits the efficiency of the pumping cycle, keeping the polarization in the few-mT regime, is not understood.

Immediately after the pump cycle, the gate voltage pattern is switched to execute one of two types of probe cycles. The first type of probe cycle starts in (2,0) and makes a short excursion into (1,1) to locate the S-T_+ resonance, allowing B_{tot} to be measured via Fig. 2A. Figure 2B shows that the nuclear polarization established by the pumping cycle relaxes over ~15 s. The second type of probe cycle starts in (2,0) and makes a long excursion deep into (1,1) to measure $P_S(\tau_S)$ where exchange is small and the S and T_0 states are mixed by $\Delta B_n^\|$. We examined $P_S(\tau_S)$ at fixed τ_S as a function of time after the end of the pump cycle by sampling V_{rf} while rastering V_L across the readout triangle. The black line in Fig. 2D shows the value of V_R, with the tick marks indicating the upper and lower limits of the rastering. Slicing through the readout triangle allows P_S to be calibrated within each slice. Remarkably, we find that $P_S(\tau_S = 25$ ns) remains close to unity—that is, the prepared singlet remains in the singlet state after 25 ns of separation—for ~15 s following the pump cycle (Fig. 2, E and F). Note that $\tau_S = 25$ ns exceeds by a factor of ~2 the value of T_2^* measured when not preceded by the pump cycle (Fig. 2C). The time after which P_S resumes its equilibrium behavior, with characteristic fluctuations [24] around an average value $P_S(\tau_S =$

25 ns) = 0.5, is found to correspond to the time for the small (~1%) nuclear polarization to relax (Fig. 2B). Measurements of $P_S(\tau_S = 25$ ns) using the same probe cycle without the preceding pump cycle (Fig. 2, H and I) do not show suppressed mixing of the separated singlet state.

Measurement of $P_S(\tau_S)$ as a function of τ_S shows that T_2^* for the separated singlet can be extended from 15 ns to 1 μs, and that this enhancement lasts for several seconds following the pump cycle. These results are summarized in Fig. 3. Over a range of values of τ_S, slices through the readout triangle (as in Fig. 2E) are sampled as a function of time after pumping, calibrated using the out-of-triangle background, and averaged, giving traces such as those in Fig. 3, B to E. Gaussian fits yield $T_2^* \sim 1$ μs for 0 to 5 s after the pump cycle and $T_2^* \sim 0.5$ μs for 10 to 15 s after the pump cycle. After 60 s, no remnant effect of the pump cycle can be seen, with T_2^* returning to ~15 ns, as before the pump cycle.

The root-mean-square amplitude of longitudinal Overhauser field difference, $\langle \Delta B_n^\| \rangle_{rms} = (h/2\pi)/g\mu_B T_2^*$, is evaluated using T_2^* values within several time blocks following the pump cycle (using data from Fig. 3A). The observed increase in T_2^* following the pump cycle is thus recast in terms of a suppression of fluctuations of $\Delta B_n^\|$ (Fig. 4A). Similarly, the S-T_+ mixing rate is used to infer the size of fluctuations of the transverse component of the Overhauser field, $\langle \Delta B_n^\perp \rangle_{rms}$. Figure 4B shows $P_S(\tau_S = 25$ ns) near the S-T_+ resonance. Unlike S-T_0 mixing, which is strongly suppressed by the pump cycle, the S-T_+ resonance appears as strong as before the pump cycle.

This suggests that the energy gap $E_n^\perp$ (Fig. 4E) is not closed by the pump cycle. Note that fluctuations in $\Delta B_n^\perp$ produce fluctuations in $E_n^\perp$, which give the S-T_+ anticrossing a width in detuning ε (Fig. 4E). Converting to a width in magnetic field via Fig. 2A gives the fluctuation amplitude $\langle \Delta B_n^\perp \rangle_{rms}$ following the pump cycle. Figure 4C shows a representative slice taken from Fig. 4B at the position indicated by the white dashed line. Gaussian fits to each 1-s slice yield mean positions m and widths w in the magnetic field, which fluctuate in time (Fig. 4D). The increase in w for short times ($t < 10$ s) reflects gate voltage noise amplified by the saturating conversion from gate voltage to effective field at large B_{tot} [25]. Beyond these first few seconds, w is dominated by fluctuations of $\Delta B_n^\perp$ but is also sensitive to fluctuations in m that result from fluctuations of $B_n^\|$ (Fig. 4E). [For $t >$ 10 s, gate voltage noise makes a relatively small (<10%) contribution to the fluctuations.] Estimating and removing the contribution due to $B_n^\|$ [25] gives an estimate of $\langle \Delta B_n^\perp \rangle_{rms}$ as a function of time following the pump cycle. These results are summarized by comparing Fig. 4A and Fig. 4F: In contrast to the strong suppression of fluctuations in $\Delta B_n^\|$ following the pump cycle, no corresponding suppression of $\langle \Delta B_n^\perp \rangle_{rms}$ is observed.

Reducing the cycle rate by a factor of ~10 reduces but does not eliminate the suppression of fluctuations of $\Delta B_n^\|$ [see [25] for a discussion of the dependence of polarization on pump cycle rate]. Also, when the pump cycle is substituted by a cycle that rapidly brings the singlet into resonance with T_0, deep in (1,1), effectively performing multiple fast measurements of $\Delta B_n^\|$, no subsequent effect on S-T_0 mixing is observed. This demonstrates that transitions involving S and T_+, rather than S and T_0, lead to the suppression of nuclear field gradient fluctuations.

The observation that an adiabatic electron-nuclear flip-flop cycle will suppress fluctuations of the nuclear field gradient has been investigated theoretically [26, 27]. These models explain some, but not all, of the phenomenology described here, and it is fair to say that a complete physical picture of the effect has not yet emerged. Other nuclear preparation schemes arising from various hyperfine mechanisms, not directly related to the specific pump cycle investigated here, have also been addressed theoretically in the recent literature [28, 29].

Control spin qubits in the presence of time-varying equilibrium Overhauser gradients require complex pulse sequences [4] or control of sizable magnetic field gradients [2, 30]. Suppressing fluctuations of $\Delta B_n^\|$ by a factor of ~100, as demonstrated here by means of nuclear state preparation, leads to an improvement in control fidelity on the order of 10^4, assuming typical control errors, which scale quadratically with the size of the fluctuating field at low-frequencies. We further anticipate generalizations of the present results using more than two confined spins, which would allow arbitrary gradients in nuclear fields to be created by active control of Overhauser coupling.
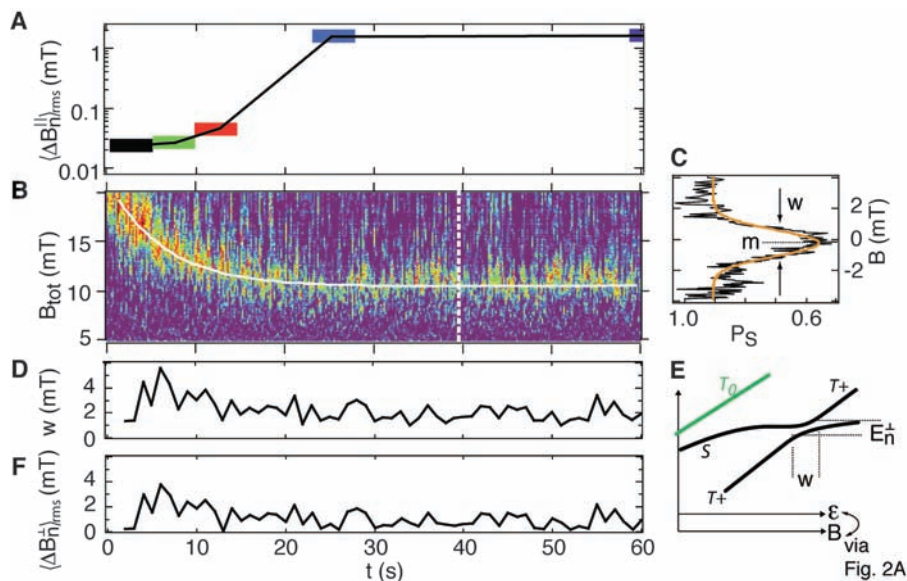
Fig. 4. (**A**) Amplitude of fluctuating longitudinal Overhauser field, $\langle \Delta B_n^\| \rangle_{rms}$, extracted from T_2^* values at the 5-s intervals in Fig. 3A. (**B**) S-T_+ resonance probed immediately after the pump cycle. Position of the resonance yields B_{tot} and its intensity gives P_S ($B_0 = 10$ mT, $\tau_S = 25$ ns). (**C**) Slice from (B) at position marked by white dashed line, averaged for 1 s. For each slice a Gaussian fit yields the mean position m and width w of the S-T_+ resonance, given in units of magnetic field via Fig. 2A. (**D**) Resonance width w as a function of time after the pumping cycle. (**E**) Schematic of the S-T_+ anticrossing, showing how fluctuations of $E_n^\perp$ due to $\Delta B_n^\perp$ give the resonance a width. (**F**) Fluctuations in $\Delta B_n^\perp$ in terms of $\langle \Delta B_n^\perp \rangle_{rms}$ in a 1-s slice.

References and Notes

1. D. Loss, D. DiVincenzo, *Phys. Rev. A* **57**, 120 (1998).
2. J. Levy, *Phys. Rev. Lett.* **89**, 147902 (2002).
3. J. M. Taylor *et al.*, *Nat. Phys.* **1**, 177 (2005).
4. J. R. Petta *et al.*, *Science* **309**, 2180 (2005); published online 1 September 2005 (10.1126/science.1116955).
5. F. H. L. Koppens *et al.*, *Nature* **442**, 766 (2006).
6. K. C. Nowack, F. H. L. Koppens, Yu. V. Nazarov, L. M. K. Vandersypen, *Science* **318**, 1430 (2007); published online 1 November 2007 (10.1126/science.1148092).
7. J. M. Elzerman *et al.*, *Nature* **430**, 431 (2004).
8. S. Amasha *et al.*, *Phys. Rev. Lett.* **100**, 046803 (2008).
9. S. I. Erlingsson, Y. V. Nazarov, V. I. Fal'ko, *Phys. Rev. B* **64**, 195306 (2001).
10. A. V. Khaetskii, D. Loss, L. Glazman, *Phys. Rev. Lett.* **88**, 186802 (2002).
11. I. A. Merkulov, A. L. Efros, M. Rosen, *Phys. Rev. B* **65**, 205309 (2002).
12. A. Imamoglu, E. Knill, P. Zoller, *Phys. Rev. Lett.* **91**, 017402 (2003).
13. D. Klauser, W. A. Coish, D. Loss, *Phys. Rev. B* **73**, 205302 (2006).
14. G. Giedke, J. M. Taylor, D. D'Alessandro, M. D. Lukin, A. Imamoglu, *Phys. Rev. A* **74**, 032316 (2006).
15. D. Stepanenko, G. Burkard, G. Giedke, A. Imamoglu, *Phys. Rev. Lett.* **96**, 136401 (2006).
16. K. Khodjasteh, D. A. Lidar, *Phys. Rev. Lett.* **95**, 180501 (2005).
17. W. Zhang, V. V. Dobrovitski, L. F. Santos, L. Viola, B. N. Harmon, *Phys. Rev. B* **75**, 201302(R) (2007).
18. W. Yao, R.-B. Liu, L. J. Sham, *Phys. Rev. Lett.* **98**, 077602 (2007).
19. A. Greilich *et al.*, *Science* **317**, 1896 (2007).
20. J. R. Petta *et al.*, *Phys. Rev. Lett.* **100**, 067601 (2008).
21. D. J. Reilly, C. M. Marcus, M. P. Hanson, A. C. Gossard, *Appl. Phys. Lett.* **91**, 162101 (2007).
22. J. M. Taylor *et al.*, *Phys. Rev. B* **76**, 035315 (2007).
23. A. C. Johnson *et al.*, *Nature* **435**, 925 (2005).
24. D. J. Reilly *et al.*, http://arxiv.org/abs/0712.4033 (2007).
25. See supporting material on *Science* Online.
26. G. Ramon, X. Hu, *Phys. Rev. B* **75**, 161301(R) (2007).
27. W. M. Witzel, S. Das Sarma, *Phys. Rev. B* **77**, 165319 (2008).
28. H. Christ, J. I. Cirac, G. Giedke, *Phys. Rev. B* **75**, 155324 (2007).
29. J. Danon, Y. V. Nazarov, *Phys. Rev. Lett.* **100**, 056603 (2008).
30. L.-A. Wu, D. A. Lidar, *Phys. Rev. Lett.* **88**, 207902 (2002).
31. We thank L. DiCarlo and A. C. Johnson for technical contributions, and W. Coish, F. Koppens, D. Loss, and A. Yacoby for useful discussions. Supported by ARO/IARPA, DARPA, and NSF-NIRT (grant EIA-0210736). Research at UCSB was supported in part by QuEST, an NSF Center.

Large Electrocaloric Effect in Ferroelectric Polymers Near Room Temperature

Bret Neese,[1,3] Baojin Chu,[1,3] Sheng-Guo Lu,[1] Yong Wang,[2] E. Furman,[1] Q. M. Zhang[1,2]*

Applying an electrical field to a polar polymer may induce a large change in the dipolar ordering, and if the associated entropy changes are large, they can be explored in cooling applications. With the use of the Maxwell relation between the pyroelectric coefficient and the electrocaloric effect (ECE), it was determined that a large ECE can be realized in the ferroelectric poly(vinylidene fluoride-trifluoroethylene) [P(VDF-TrFE)] copolymer at temperatures above the ferroelectric-paraelectric transition (above 70°C), where an isothermal entropy change of more than 55 joules per kilogram per kelvin degree and adiabatic temperature change of more than 12°C were observed. We further showed that a similar level of ECE near room temperature can be achieved by working with the relaxor ferroelectric polymer of P(VDF-TrFE-chlorofluoroethylene).

When an electric field is applied to a dielectric material, it will induce a change in the material's polarization. The consequent changes in the entropy and temperature of the material are referred to as the electrocaloric effect (ECE) (*1–7*). The ECE may provide an efficient means to realize solid-state cooling devices for a broad range of applications such as on-chip cooling and temperature regulation for sensors and electronic devices, provided that materials with large ECE can be developed. Refrigeration based on the ECE approach is more environmentally friendly and hence may also provide an alternative to the existing vapor-compression approach.

A large ECE requires a large entropy change associated with the polarization change, and the dielectric material must be capable of generating large polarization changes. These requirements make it advantageous to use ferroelectric materials for the ECE and to operate the materials in a temperature region above a ferroelectric (polarization ordered)–paraelectric (polarization-disordered) (F-P) phase transition, where large electric field–induced polarization changes can be achieved (*1*, *2*). Jona and Shirane showed that the ECE occurs in both ferroelectric and paraelectric phases, and the effect is larger in the paraelectric phase just above the F-P transition (*2*). Recently "giant" ECEs were reported in ferroelectric ceramic Pb(Zr$_{0.95}$Ti$_{0.05}$)O$_3$ thin films at temperatures near and above the F-P transition (*6*). These results are also consistent with experimental results regarding the magnetocaloric effect (MCE) in ferromagnetic materials, in which a giant MCE was observed at temperatures above the ferromagnetic-paramagnetic transition (*8–14*).

In an ideal refrigeration cycle, the working material must absorb entropy from the load to be cooled while it is in thermal contact with the load

[isothermal entropy change (ΔS)]. The material is then isolated from the load while the temperature is increased because of an increased applied electric field [adiabatic temperature change (ΔT)]. The material is then placed in thermal contact with the heat sink, and the entropy that was absorbed from the cooling load is transferred to the heat sink. The working material is then isolated from the heat sink and its temperature is reduced back to the temperature of the cooling load as the field is reduced and the process is repeated. Thus, both ΔS and ΔT are the key parameters for the ECE of a dielectric material for use in refrigeration (*1*, *2*, *8–12*).

Although large ΔT of ~12°C has been reported in ferroelectric ceramics at about 230°C, the ΔS [~8 J per kilogram per kelvin degree (J/(kgK)] was not as high as that observed in magnetic materials that exhibit a giant MCE near room temperature, where ΔS higher than 30 J/(kgK) was observed (*6*, *8*, *11*). An underlying reason for the small ΔS is that the small ionic displacements in these ferroelectric ceramics may not generate large entropy changes. However, the ordering and disordering of dipoles in ferroelectric polymers can result in a large entropy change. For example, the heat of the F-P transition for the ferroelectric polymer poly(vinylidene fluoride-trifluoroethylene) [P(VDF-TrFE)] [65/35 mole % (mol %)] is >20.9 kJ/kg [or ΔS ~ 56 J/(kgK)], which is even greater than that of the recently reported giant MCE (*15*). Furthermore, these normal ferroelectric polymers have been converted to ferroelectric relaxors that exhibit a very slim electric displacement-electric field (D-E) loop near room temperature with large electric field–induced polarization, suggesting a giant ECE near room temperature (*16–18*).

We investigated the ECE in normal ferroelectric P(VDF-TrFE) (55/45 mol %) at temperatures above the F-P transition and in the relaxor ferroelectric polymer P(VDF-TrFE-chlorofluoroethylene) [P(VDF-TrFE-CFE)] at near room temperature around the dielectric constant maximum. We chose the P(VDF-TrFE) (55/45 mol %) copolymer be-

[1]Materials Research Institute, The Pennsylvania State University, University Park, PA 16802, USA. [2]Electrical Engineering Department, The Pennsylvania State University, University Park, PA 16802, USA. [3]Materials Science and Engineering Department, The Pennsylvania State University, University Park, PA 16802, USA.

*To whom correspondence should be addressed. E-mail: qxz1@psu.edu